JACS
JOURNAL OF THE AMERICAN CHEMICAL SOCIETY

Role of Support–Nanoalloy Interactions in the Atomic-Scale Structural and Chemical Ordering for Tuning Catalytic Sites

Lefu Yang,[†] Shiyao Shan,[†] Rameshwori Loukrakpam,[†] Valeri Petkov,[‡,*] Yang Ren,[⊥] Bridgid N. Wanjala,[†] Mark H. Engelhard,[§] Jin Luo,[†] Jun Yin,[†] Yongsheng Chen,[¶] and Chuan-Jian Zhong[†,*]

[†]Department of Chemistry, State University of New York at Binghamton, Binghamton, New York 13902, United States

[‡]Department of Physics, Central Michigan University, Mt. Pleasant, Michigan 48859, United States

[§]EMSL, Pacific Northwest National Laboratory, Richland, Washington 99352, United States

[⊥]Advanced Photon Source, Argonne National Laboratory, Argonne, Illinois 60439, United States

[¶]EMS Energy Institute and Department of Energy and Mineral Engineering, Pennsylvania State University, University Park, Pennsylvania 16802, United States

Supporting Information

ABSTRACT: The understanding of the atomic-scale structural and chemical ordering in supported nanosized alloy particles is fundamental for achieving active catalysts by design. This report shows how such knowledge can be obtained by a combination of techniques including X-ray photoelectron spectroscopy and synchrotron radiation based X-ray fine structure absorption spectroscopy and high-energy X-ray diffraction coupled to atomic pair distribution function analysis, and how the support-nanoalloy interaction influences the catalytic activity of ternary nanoalloy (platinum–nickel–cobalt) particles on three different supports: carbon, silica, and titania. The reaction of carbon monoxide with oxygen is employed as a probe to the catalytic activity. The thermochemical processing of this ternary composition, in combination with the different support materials, is demonstrated to be capable of fine-tuning the catalytic activity and stability. The support-nanoalloy interaction is shown to influence structural and chemical ordering in the nanoparticles, leading to support-tunable active sites on the nanoalloys for oxygen activation in the catalytic oxidation of carbon monoxide. A nickel/cobalt-tuned catalytic site on the surface of nanoalloy is revealed for oxygen activation, which differs from the traditional oxygen-activation sites known for oxide-supported noble metal catalysts. The discovery of such support–nanoalloy interaction-enabled oxygen-activation sites introduces a very promising strategy for designing active catalysts in heterogeneous catalysis.

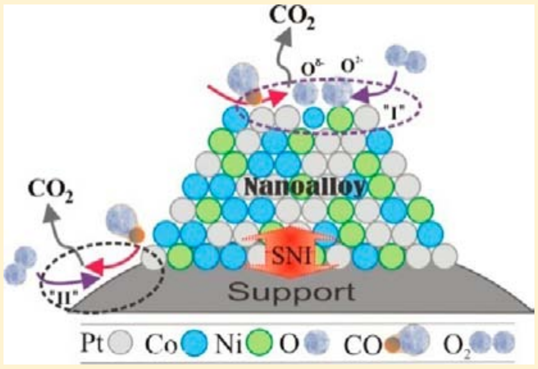

1. INTRODUCTION

To design active, robust, and low-cost alloy catalysts for technologically useful applications, including green energy storage and conversion devices,[1,2] recent studies have focused on increasing the catalyst's activity and stability while reducing the amount of Pt by alloying it with different transition metals, in particular for an oxygen reduction reaction.[3−41] In addition to bimetallic alloys, such as Pt−Co or Pt−Ni alloys,[28,34−40] increasing attention is being paid to ternary alloy catalysts following the mounting evidence that they can deliver even better performance in activity and stability at a much lower Pt content in the catalysts.[3−10,14,15,19,20,28−32,41] The enhancement has been mostly attributed to lattice strain brought about by the alloying as manifested by changes in the lattice parameter of a face centered cubic (fcc) type structure.[10,29,41] More often than not, however, nanoalloy catalysts are deposited on supports as catalysts in important chemical reactions such as, for example, preferential oxidation (PROX) of carbon monoxide in a water gas shift (WGS) reaction for hydrogen production.[42−46] Since conventional understanding of support-metal interactions (SMI) in heterogeneous catalysis provides little insight about supported nanoalloys[47−49] a fundamental question arises then about the role of the support–nanoalloy interactions (SNI) in determining the structures of the supported nanoalloys, including the type of chemical and structural ordering, the degree of local structural deformation/strain etc., and hence, their correlation with catalytic activity. Answering this question is thus significant for developing the rationale design of nanosized catalysts given the abundant demonstrations of nanosynthesis techniques.

We address this question by concentrating on the oxidation reaction of carbon monoxide with oxygen as a model probe to the active sites on the supported nanoalloy catalyst, as depicted in Scheme 1. The CO activation on the Pt active site is hypothesized to be coupled to oxygen-activation sites provided

Received: June 19, 2012
Published: August 31, 2012

ACS Publications

dx.doi.org/10.1021/ja3060035 | *J. Am. Chem. Soc.* 2012, 134, 15048−15060

Scheme 1. A Schematic Illustration of the Oxidation Reaction of Carbon Monoxide with Oxygen as a Probe Reaction to the Active Sites on a Supported Nanoalloy Catalyst

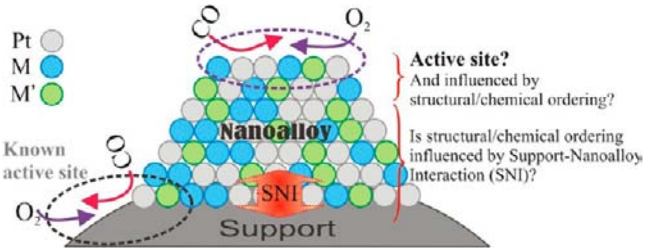

by the second/third metal (M/M′) sites in the Pt−nanoalloy. This type of oxygen-activation sites (Type-I site) is different from the anionic oxygen deficiency sites located at the nanoalloy-support perimeter zone (Type-II site).[49−55] Probing the catalytic activity of these two types of sites requires a careful consideration of the oxygen storage/release capacity of the catalyst. Conceptually, it may occur on the support and/or on the nanoalloy particles, the latter of which is provided by M and M′ metals in the nanoalloy. For achieving a high catalytic activity, the oxygen−M/M′ interaction should be strong enough for oxygen activation but not too strong to poison the binding sites. While there are extensive studies on Type-II sites, little is known about whether Type-I sites exist on the nanoalloys and how they are affected by the SNI, which is an important focus of this work.

Though not specifically for catalytic CO oxidation reaction, the rationale for the study of ternary catalysts stems from some theoretical and experimental grounds shown recently for electrocatalytic oxygen reduction reaction (ORR).[14,16,23,56−60] Experimentally, some trimetallic nanoparticle catalysts have been shown to exhibit higher electrocatalytic activity than bimetallic counterparts in recent work.[16] This finding is also supported by a Pareto optimization analysis (an optimality trade-off analysis in terms of stability and activity) (Supporting Information, Figure S1A) of existing combinatorial screening with a 16-array of thin film bimetallic catalysts,[23,56,57] from which NiCoPt is identified as a possible ternary catalyst with high activity and medium stability. Indeed, PtNiCo nanoparticles have been demonstrated in our recent work as a highly active catalyst with reasonable stability for ORR.[16] Theoretically, the volcano curve established for the activity vs affinity for oxygen in terms of binding energy of oxygen or hydroxyl (ΔE_O)[58,59] gives a value of 0.22 eV for an optimal activity that is more positive than that of Pt. With the use of the data for a binary surface alloy in which a solute metal alloyed into the surface layer of a homogeneous host metal,[58] a 3-atom model of PtM on a substrate (M′) (Supporting Information, Figure S1B) would show an active ternary PtNiCo in the region of ΔE_O values near ~2 eV for binary PtNi, and PtCo. Indeed, PtNiCo was recently demonstrated to show a higher activity for ORR than PtCo and PtNi.[14,16]

In this work the results of our study of the CO oxidation reaction reveal that the SNI plays an important role in influencing Type-I active sites in a ternary nanoalloy model system (PtMM′, where M or M′ represents base transition metals, here Ni and Co). As discussed above, with the combination of Pt−Ni−Co, it is anticipated that both activity and stability can be enhanced. This insight is obtained by a combination of techniques including X-ray photoelectron spectroscopy (XPS), synchrotron radiation based X-ray absorption near edge structure (XANES)/X-ray fine structure absorption spectroscopy (XAFS), and high-energy X-ray diffraction (HE-XRD) coupled to atomic pair distribution functions (PDFs) analysis. While XANES/XAFS provides information on the local atomic coordination structure, HE-XRD/PDF analysis provides information about the ordering of different atoms in the alloy. The ternary PtNiCo nanoparticles with very well-defined size and composition were prepared and deposited on three different and widely used supports: carbon, silica, and titania. The results indicate substantial differences in the atomic-scale structural and chemical ordering features for the three types of supported nanoalloy catalysts, which provides new insights into Type-I active sites on the nanoalloys and their catalytic activity.

2. EXPERIMENTAL SECTION

Chemicals. Platinum(II) acetylacetonate ($Pt(acac)_2$, 97%) and nickel(II) acetylacetonate ($Ni(acac)_2$, anhydrous, >95%) were purchased from Alfar Aesar. Cobalt(III) acetylacetonate ($Co(acac)_3$, 99.95%) was purchased from Strem Chemicals; 1,2-hexadecanediol (90%), octyl ether (99%), oleylamine (70%), and oleic acid (99+%) were purchased from Aldrich. Silica gel (syloid 74) was purchased from Aldrich and used as received. TiO_2 powders (P25, 25 nm size, 80% anatase, and 20% rutile) were obtained from Degussa, Germany, and used as received. Gases of CO (1 vol % balanced by N_2) and O_2 (20 vol % balanced by N_2) were purchased from Airgas. All chemicals were used as received. Pt/C (particle size ca. 2.5−3 nm) was obtained from E-tek.

Synthesis. The synthesis of PtNiCo nanoparticles involved the reaction of three metal precursors, $Pt^{II}(acac)_2$, $Ni^{II}(acac)_2$, and $Co^{III}(acac)_3$, in controlled molar ratios in an octyl ether solvent using oleylamine and oleic acid as capping agents and 1,2-hexadecanediol as a reducing agent.[61] Briefly for synthesis of $Pt_{39}Ni_{22}Co_{39}$, 4.88 mmol of 1,2-hexadecanediol, 3.26 mmol of $Co(acac)_3$, 2.88 mmol of $Ni(acac)_2$, 3.51 mmol of $Pt(acac)_2$, 6.4 mmol of oleylamine, 9.4 mmol of oleic acid, and 450 mL octyl ether were added to a 3-neck 1 L flask under vigorous stirring. The solution was heated to 280 °C, and refluxed for 40 min. The nanoparticle product was dispersed in a known amount of hexane. PtCo and PtNi nanoparticles were also synthesized similarly, which are detailed in a previous report.[14]

Catalysts Preparation. The nanoparticles were supported on three different support materials. For the preparation of carbon supported nanoparticles, a typical procedure involved suspending 900 mg of carbon black (Ketjen Black) in 500 mL of hexane containing ~300 mg of nanoparticles followed by stirring for approximately 15 h. The resulted powder was collected and dried under N_2. The silica or titania supported catalysts were prepared similarly, where the support was pretreated at 500 °C for 2 h.

The supported catalysts were further treated in a quartz tube furnace. The nanoparticles supported on carbon were treated by two different processes. In one process, the catalyst was first heated at 260 °C in N_2 (nonreactive atmosphere) for 30 min for removing the organic capping molecules, and then treated at 400 °C in 15 vol % H_2 for 120 min. In the other process, the catalyst was first heated at 260 °C in 15 vol % O_2 (oxidative atmosphere) for 30 min for removing the capping molecules, and then treated at 400 °C in 15 vol % H_2 for 120 min. The silica (SiO_2) and titania (TiO_2) supported samples were also first treated at 260 °C in 15 vol % O_2 for 30 min for removing the capping molecules, and then annealed at 400 °C in 15 vol % H_2 for 120 min. This synthesis-processing protocol resulted in all samples having virtually the same trimetallic composition. In the case of titania and silica supports the nanoparticle catalysts loading was 5 wt %; the loading of the carbon supported catalysts was 20 wt %. The particle sizes of the carbon-supported catalysts were 4.4 ± 0.5 nm for $Pt_{39}Ni_{22}Co_{39}$/C, 3.5 ± 0.4 nm for $Pt_{25}Ni_{16}Co_{59}$/C, 3.9 ± 0.7 nm for $Pt_{45}Co_{55}$/C, and 8.7 ± 0.8 nm for $Pt_{64}Ni_{36}$/C.

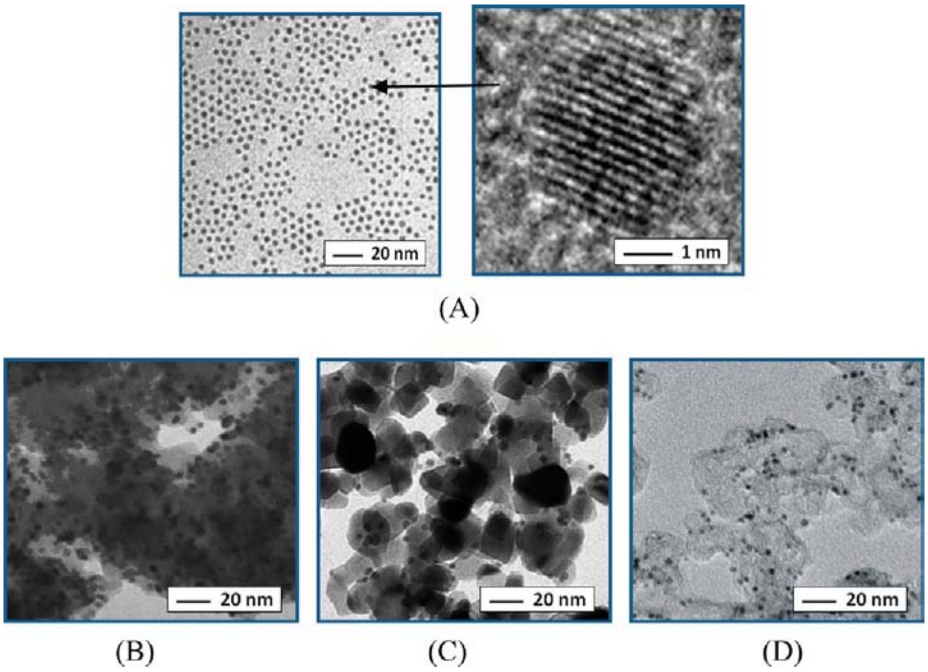

(A)

(B) (C) (D)

Figure 1. TEM images for (A) as-synthesized $Pt_{39}Ni_{22}Co_{39}$ nanoparticles, 3.4 ± 0.4 nm; (B) $Pt_{39}Ni_{22}Co_{39}/SiO_2$, 4.8 ± 0.6 nm; (C) $Pt_{39}Ni_{22}Co_{39}/TiO_2$, 5.2 ± 0.7 nm; (D) $Pt_{39}Ni_{22}Co_{39}/C$,4.4 ± 0.5 nm.

Characterization of Catalysts. Transmission electron microscopy (TEM) was performed on Hitachi H-7000 electron microscope (100 kV) to determine the particle size and size distribution.

Inductively coupled plasma−optical emission spectroscopy (ICP−OES) was used to analyze the composition, which was performed using a Perkin-Elmer 2000 DV ICP−OES utilizing a cross-flow nebulizer with the following parameters: plasma, 18.0 L $Ar_{(g)}$/min; auxiliary, 0.3 L $Ar_{(g)}$/min; nebulizer, 0.73 L $Ar_{(g)}$/min; power, 1500 W; peristaltic pump rate, 1.40 mL/min. Elements <1.0 mg/L were analyzed using a Meinhardt nebulizer coupled to a cyclonic spray chamber to increase analyte sensitivity with the following parameters: 18.0 L $Ar_{(g)}$/min; auxiliary, 0.3 L $Ar_{(g)}$/min; nebulizer, 0.63 L $Ar_{(g)}$/min; power, 1500 W; peristaltic pump rate, 1.00 mL/min. Laboratory check standards were analyzed every 6 or 12 samples, with instrument recalibration if check standards were not within ±5% of the initial concentration. Note that the composition of the supported nanoparticles after thermal treatment was sometimes slightly different (<10%) from that of the as-synthesized nanoparticles (e.g., a composition of $Pt_{36}Ni_{29}Co_{35}$ supported on carbon was obtained for the as-synthesized $Pt_{39}Ni_{22}Co_{39}$), which were largely due to different degrees of losses of metals into the supporting materials during ICP sample preparation.

Thermogravimetric analysis (TGA) was performed on a Perkin-Elmer Pyris 1-TGA for determining the weight of the organic shells.

The catalytic activity of the catalysts for CO (1 vol % balanced by N_2) + O_2 (20 vol % balanced by N_2) reaction was measured using a custom-built system including a temperature-controlled reactor, gas flow/mixing/injection controllers, and an online gas chromatograph (Shimadzu GC 8A) equipped with 5A molecular sieve and Porapak Q packed columns and a thermal conductivity detector. The catalytic activity for CO oxidation was determined by analyzing the composition of the tail gas effusing from the quartz microreactor packed with catalyst fixed bed. Both pretreatment and aging tests were carried out in this reaction system.

Synchrotron high-energy XRD measurements were carried out with both ex situ and in situ modes at the beamlines 11IDC and 11IDB, respectively, at the Advanced Photon Source, Argonne, using X-rays of energy 115 keV (λ = 0.1078 Å). The XRD diffraction data were reduced to the so-called structure factors, $S(q)$, and then Fourier transformed to the atomic PDFs $G(r)$, using the relationship

$$G(r) = \frac{2}{\pi}\int_{q=0}^{q_{\max}} q[S(q) - 1]\sin(qr)\,dq \tag{1}$$

where $q_{\max}$= 25 $Å^{-1}$ in the present experiments. The wave vector q is defined as $q = 4\pi\sin(\theta)/\lambda$, where θ is half of the scattering angle and λ is the wavelength of the X-rays used. Note, as derived, atomic PDFs $G(r)$ are experimental quantities that oscillate around zero and show positive peaks at real space distances, r, where the local atomic density $\rho(r)$ exceeds the average one ρ_o. This behavior can be expressed by the equation $G(r) = 4\pi r\rho_o[\rho(r)/\rho_o - 1]$, which is the formal definition of the PDF $G(r)$. High-energy XRD and atomic PDFs have already proven to be very efficient in studying the atomic-scale structure of nanosized materials.[62,63] In situ monitoring of the structural changes of selected catalysts were also performed using a reactor-type cell described by Oxford et al.[64] The in situ studies were done at the beamline 11IDB using X-rays of energy 90 keV (λ = 0.1378 Å). The respective XRD patterns were also processed in atomic PDFs.

XPS measurements were performed ex-situ using a Physical Electronics Quantum 2000 scanning ESCA microprobe. This system uses a focused monochromatic Al Kα X-ray (1486.7 eV) source for excitation and a spherical section analyzer. The instrument has a 16-element multichannel detection system. The X-ray beam used was a 100 W, 100-μm in diameter beam. It was rastered over a 1.4 mm by 0.2 mm rectangle spot on the sample. The X-ray beam was incident normal to the sample, and the X-ray detector was at 45° away from the normal. The binding energy (BE) scale was calibrated using a Cu $2p_{3/2}$ peak at 932.62 eV and Au $4f_{7/2}$ peak at 83.96 eV from known standards. The percentages of individual elements detected were determined by analyzing the areas of the respective peaks.

X-ray absorption fine structure (XAFS) spectra (Pt L3 edge (11,564 eV), Co K edge (7,709 eV) and Ni K edge (8,333 eV)) were collected (ex-situ) on the bending magnet beamline 9-BM-B at the Advanced Photon Source, Argonne National Laboratory. Near-edge region or X-ray absorption near edge structure (XANES) spectra were processed using Athena.[32] The fitting was limited to 2.0−12.5 $Å^{-1}$ for Ni and Co K edge spectra, using a Hanning window with dk =1.0 $Å^{-1}$. The fits were performed to both the real and imaginary parts of $\chi(R)$ in the region of 1.0 < R < 3.2 Å. Similar analysis was also performed on reference samples of Pt, Ni, and Co foils to obtain S_0^2, the amplitude reduction factor, for the subsequent determination of the coordination

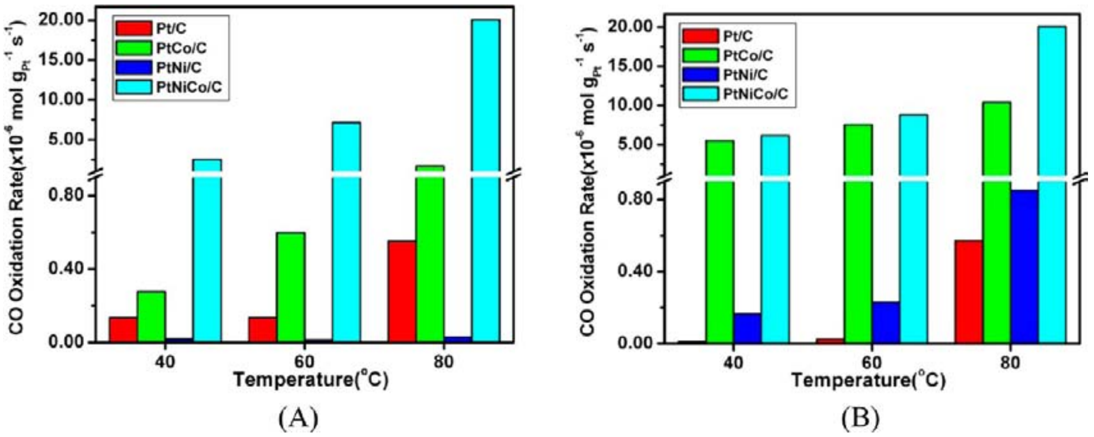

Figure 2. Comparisons of Pt mass specific CO oxidation rates of $Pt_{39}Ni_{22}Co_{39}/C$ with those of $Pt_{64}Ni_{36}/C$, $Pt_{45}Co_{55}/C$, and Pt/C catalysts at two different states: as-prepared (A) and reactivated states (B). (The as-prepared catalyst (A) underwent thermochemical treatment first under O_2 or N_2 (260 °C) and then H_2 (400 °C) followed by exposure to ambient air for an extensive period of time before the catalytic measurement; the reactivated catalyst (B) was reactivated in situ under H_2 at 400 °C before the catalytic measurement. The standard deviation of the data is $\pm 0.06 \times 10^{-6}$ mol g_{Pt}^{-1} s^{-1}, 0.4% RSD). The Pt mass specific CO oxidation rate is normalized against the metal loading on carbon and the Pt composition in the nanoparticles.

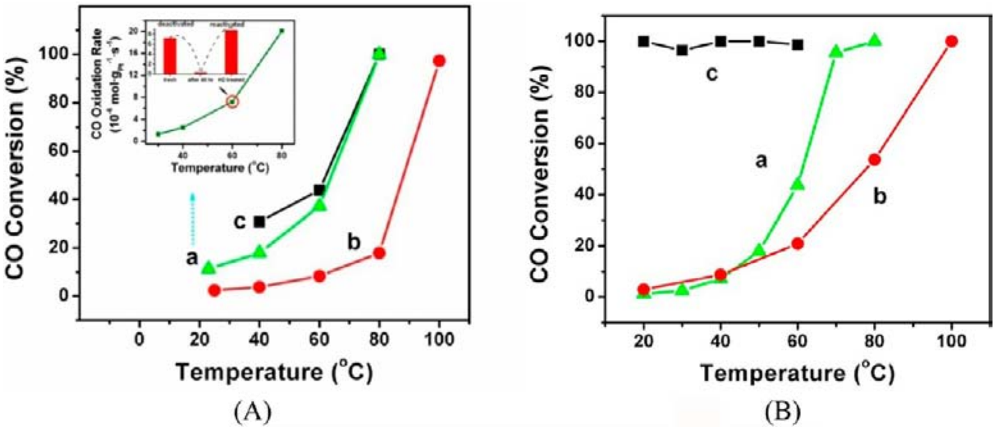

Figure 3. CO conversion activities vs reaction temperature. (A) Activities for (a) initial, (b) oxidized (20 vol % O_2, 260 °C, 1 h), and (c) reduced (15 vol % H_2, 400 °C, 1 h) states of $Pt_{39}Ni_{22}Co_{39}/C$ catalyst. This catalyst was initially prepared by treatment at 260 °C in N_2 followed by treatment at 400 °C in 15 vol % H_2. Insert: comparison of oxidation rates (mol g_{Pt}^{-1} s^{-1})) between the initial, the deactivated (48 h after reaction under CO + O_2), and the reactivated (1 h after H_2 reduction) catalysts. (Oxidation rate = $(PV/RT \times C_{CO})/(m_{catalyst} \times \text{wt\% (loading)} \times 60)$). (B) Activities of (a) initial, (b) oxidized (20 vol % O_2, 260 °C, 1 h), and (c) reduced (15 vol % H_2, 400 °C, 1 h, following reaction under CO + O_2) states of $Pt_{25}Ni_{16}Co_{59}/C$ catalyst prepared by treatment at 260 °C under 20 vol % O_2 (oxidative) followed by treatment at 400 °C in 15 vol % H_2 (reductive) in the fixed bed reactor. (The standard deviation of the data is ±0.3%, with an RSD of 0.4%).

numbers of the fitted structure of the samples. The S_0^2 values for Pt, Ni, and Co were determined to be 0.84, 0.81, and 0.74, respectively.

3. RESULTS AND DISCUSSION

As shown in Figure 1A, the as-synthesized PtNiCo nanoparticles are highly monodispersed with a good crystallinity. While loadings of PtNiCo nanoparticles on support vary, the average particle size changes very little with the support type (4.4 nm for carbon to 4.8 nm for SiO_2 and to 5.2 nm for TiO_2) (Figure 1B).

3.1. Catalytic Activities. The CO conversion rates of PtNiCo/C catalyst were first compared with those from samples of PtCo/C and PtNi/C catalysts at different reaction temperatures in terms of Pt-specific mass activity (Figure 2). The data for a sample of E-tek's Pt/C catalyst is also included for comparison. The comparison was performed for a selected set of alloy compositions to illustrate the importance of the ternary alloy for enhancing the catalytic activity.

In Figure 2, the catalytic CO conversion rates of the ternary PtNiCo/C catalyst are compared with those of the binary PtNi/C and PtCo/C in both an as-prepared state (Figure 2A, i.e., the catalyst underwent thermochemical treatment first under O_2 and then H_2 followed by exposure to ambient air for more than one week) and a reactivated state (Figure 2B, i.e., the catalyst was reactivated in situ under H_2). The data for a sample of E-tek's Pt/C catalyst is also included for the comparison. For the as-prepared catalyst, which is likely partially oxidized at the surface by air, PtNiCo has an activity higher than PtCo and PtNi. The activity of PtCo is slightly higher than that of Pt, whereas PtNi has almost no activity. Interestingly, upon reactivation in situ by H_2, which reduces the particles back to alloy state, the activity for the ternary catalyst shows an increase by a factor of 2−3. PtCo shows the largest increase in activity (by a factor of 10−20), though being still lower than the ternary catalyst, especially at the high reaction temperature. In contrast, PtNi shows practically no change in

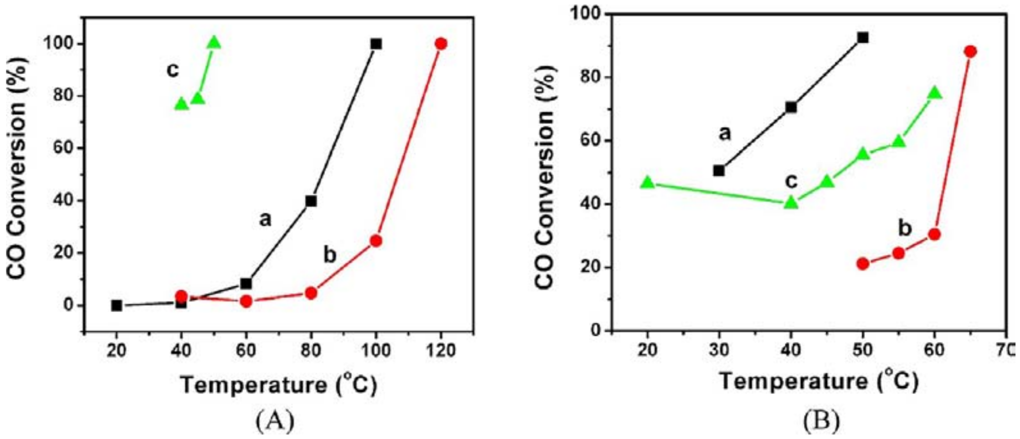

Figure 4. (A) CO conversion as a function of the reaction temperature for $Pt_{39}Ni_{22}Co_{39}/SiO_2$ catalyst: (a) initial, (b) oxidized (48 h after reaction under CO + O_2 atmosphere), and (c) reduced (15 vol % H_2, 400 °C, 1 h) from oxidized sample. (B) CO conversion as a function of the reaction temperature for $Pt_{39}Ni_{22}Co_{39}/TiO_2$: (a) initial, (b) oxidized (48 h under CO + O_2), and (c) H_2-reduced (15 vol % H_2, 400 °C, 1 h) catalysts. (The standard deviation of the data is ±0.3%, with an RSD of 0.4%).

activity, similar to Pt. Note that the observed trends of catalytic activity remain unchanged even by taking the differences in particle sizes into consideration, as reflected by a comparison of the surface Pt-specific catalytic activities of these catalysts (Supporting Information, Table S1).

As will be discussed in details, on the basis of the structural characterization results, not only the degree of alloying but also the alloy composition have played important roles in the enhancement of the catalytic activity, which can be understood by considering a combination of several factors, including the propensity of oxidation of the metals in the presence of oxygen, the reduction potentials of the metals, the structure of the alloying, and most importantly the surface activation of oxygen for the catalytic CO oxidation reaction. The alloying of Pt with Co imparts the catalyst with an enhanced capability for the activation of the oxygen species, which explains the fact that PtCo/C after reactivation has much higher catalytic activity than pure Pt/C. In contrast, the likely significantly oxidized surface as-prepared PtCo/C in the ambient atmosphere led to poisoning of the oxygen-activation sites, which explains the observed activity being similar to that of Pt/C. In comparison, Ni alloyed in Pt had apparently little effect on the catalytic activity, which is probably due to less propensity of surface oxidation or oxygenation than that of Co (E^0 = −0.25 and −0.28 V for Ni and Co, respectively), explaining its low activity and insensitivity to the exposed atmosphere. These two attributes, that is, the higher propensity of Co and the lower propensity of Ni to surface oxidation or oxygenation, are apparently taken advantage of, as reflected by the relative high stability of the as-prepared ternary PtNiCo catalyst in ambient condition and the catalytic activity higher than those of the bimetallic counterparts. This type of synergy for stabilizing the active Co species in the alloy while promoting the surface oxygenation for the oxygen activation will be further discussed along with the structural characterization data.

The change of the CO conversion rate over the nanoalloy catalyst at different reaction temperatures was examined (Figure 3). For $Pt_{39}Ni_{22}Co_{39}/C$ (Figure 3A), the initial activity was relatively high (a), which was found to drop significantly after the oxidation pretreatment for 1 h at 200 °C (b). By exposing the same nanoalloy to a reduction condition, there was clearly recovery of the activity, basically comparable to the initial one. These observations indicate that the nanoalloy was deactivated in the oxidizing atmosphere and reactivated upon exposure to the reducing atmosphere. This fact was further substantiated by significant reduction in activity for the deactivated nanoalloy under CO + O_2 atmosphere at 60 °C for 48 h, and the return of activity to its initial values upon H_2 treatment (Figure 3A insert).

The change in the catalytic activity was shown to depend on the nanoalloy composition. For example, a sample of $Pt_{25}Ni_{16}Co_{59}/C$ was annealed 260 °C under 20 vol % O_2 (air) for 1 h followed by 15 vol % H_2 at 400 °C for 1 h in the fixed bed reactor. The initial catalytic activity was relatively high, but it decreased rapidly within 1 h, showing a steady catalytic activity (Figure 3B,a). This was followed by reducing the catalyst under 15 vol % H_2 at 400 °C for 1 h (Figure 3B,c). Clearly, the catalytic activity showed a significant increase (Figure 3B,c) from its initial value (Figure 3B,a) upon the reduction treatment. In comparison with the data for $Pt_{39}Ni_{22}Co_{39}/C$ (Figure 3A,c), the catalytic activity for $Pt_{25}Ni_{16}Co_{59}/C$ showed a higher catalytic activity after hydrogen reduction (Figure 3B,c). However, a significant deactivation was also observed for $Pt_{25}Ni_{16}Co_{59}/C$ in the reaction atmosphere, in contrast to the relatively insignificant deactivation for $Pt_{39}Ni_{22}Co_{39}/C$ (Supporting Information, Figure S2). These differences between $Pt_{25}Ni_{16}Co_{59}/C$ and $Pt_{39}Ni_{22}Co_{39}/C$ were believed to reflect the difference between the two samples in the amount of base metal atoms surrounding Pt atoms on the surface of the nanoalloy. Since the amount of base metals for $Pt_{25}Ni_{16}Co_{59}/C$ is larger than that for $Pt_{39}Ni_{22}Co_{39}/C$, the former may favor the catalytic activation of oxygen species, but could suffer from a loss of the activity due to propensity of the base metal oxidation under the oxidative reaction condition. As a result, the difference between initial activity (a) and the activity upon oxidation (b) for $Pt_{25}Ni_{16}Co_{59}/C$ is smaller than that for $Pt_{39}Ni_{22}Co_{39}/C$.

Three different supports were compared to assess the catalytic activity of the nanoalloy catalysts. For CO conversion over $Pt_{39}Ni_{22}Co_{39}/SiO_2$ (Figure 4A), a low catalytic activity was observed (Figure 4A,a), reflecting likely a poor activity for oxygen activation. There was also a significant deactivation after the oxidation reaction (CO + O_2) (Figure 4A,b). Upon a complete H_2-reduction of the catalyst treated under O_2, the activity increases significantly (Figure 4A,c). As will be discussed later, oxygen activation occurs by the formation of surface oxygenated base transition metals at the alloy sites (Type-I), which could be depleted by a full oxidation of the base transition metals.

In contrast to carbon and SiO_2 supports, a high initial activity was observed for $Pt_{39}Ni_{22}Co_{39}/TiO_2$ catalyst (Figure 4B,a). However, this activity was found to drop significantly after the oxidation reaction for a certain period of time (Figure 4B,b). Upon H_2-reduction, the activity was also quite high initially, and shows only a moderate increase with increasing reaction temperature (Figure 4B,c). Unlike the cases of C and SiO_2 supports, TiO_2 is a well-known "active" support. Under H_2 a reduction of Ti(IV) to Ti(III) takes place, which may have contributed to the observed inability to completely reactivate the catalyst.

The catalytic activity of titania supported nanoalloy was analyzed in terms of the base transition metal assisted platinum site, the so-called Type-I site, and the perimeter zone of the TiO_2 support around the nanoalloy particle, the so-called Type-II site.[49,51] At low temperature, the consumption of the activated oxygen from the catalyst's perimeter zone may not be well balanced by the supply. In this case, Type-I sites are mainly responsible for the observed activity. However, the activation sites from the perimeter zone become effective at elevated reaction temperature (e.g., 65 °C). Since there was no apparent decay of activity over time, it may be concluded that Type-II sites maintained a stable supply of activated oxygen at higher reaction temperatures.

SiO_2 is known to be insensitive to H_2 reduction atmosphere, whereas titania is reducible by H_2. In the case of carbon, H_2 can only reduce surface oxygenated species. The observed increase in the activity for the SiO_2 supported catalyst upon H_2 reduction suggests a certain degree of reconstruction of the nanoalloy, leading possibly to the presence of Type-I active sites on the nanoalloy. In the case of TiO_2 supported nanoalloy subjected to H_2 reduction, the activity is initially slightly higher than that for SiO_2 support, but drops rather fast in time. The decrease of the activity could be due to the reduction of TiO_2 support along with the reduction of the oxygenated species on the nanoalloy, thus diminishing the activity of Type-II sites. Indeed, H_2 pretreatment was previously shown to result in a strong support−metal interaction involving Pt and Ti^{3+} that induces a decrease of the adsorption efficiency of the reactant molecules.[47] The fact that the initial activity follows the order of TiO_2 > carbon > SiO_2 suggests that the two types of oxygen-activation sites (I and II) could have contributed to the observed variations. It also indicates that SNI can influence the catalytic activity to a very substantial extent.

3.2. HE-XRD and Atomic PDFs Characterization.

Figure 5 shows the HE-XRD patterns (A) and the respective atomic PDFs (B) for $Pt_{39}Ni_{22}Co_{39}$ nanoalloys supported on the three different supports. The XRD patterns show broad diffraction features that are typical for nanosized particles and difficult to analyze unambiguously in the traditional way.

The respective PDFs show a sequence of sharp peaks, reflecting the presence of well-defined atomic coordination spheres in all three samples studied, allowing convenient testing and refinement of structure models. The radii of the coordination spheres can be estimated from the positions of the respective PDF peaks, and the coordination numbers can be estimated from the areas of those peaks. The real space distance at which the atomic PDF decays to zero is a measure of the so-called length of structural coherence, also known as coherently scattering domain size. In particular, the peaks in the experimental PDFs in Figure 5 show up to a real space distance of about 25−35 Å, which may be considered as a length of structural coherence in the nanoalloy particles studied here. That length is comparable to but less than the particles' size (~5 nm) determined by TEM, indicating the presence of non-negligible local atomic disorder in the nanoalloys. The presence of such disorder is typical for metallic particles a few nanometer in size and usually is due to surface relaxation effects.[65,66]

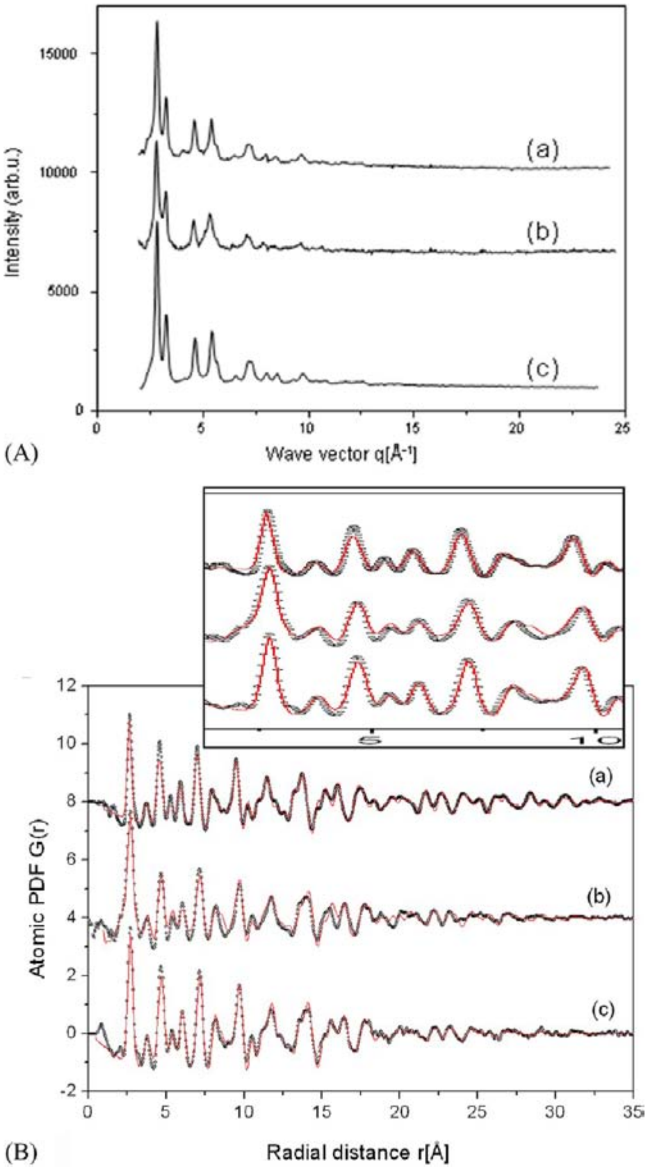

Figure 5. High-energy XRD patterns (A), and atomic PDFs (B) for $Pt_{39}Ni_{22}Co_{39}$ nanoalloys supported on (a) carbon, (b) SiO_2, and (c) TiO_2. All three catalysts were treated by the same protocol, that is, treatment at 260 °C in 15 vol % O_2 followed by treatment at 400 °C in 15% H_2. Results from PDF modeling (B, line in red) are explained in the text. (Insert: a zoomed view of the data in the lower radial distance region).

In Figure 6, the atomic PDFs for $Pt_{39}Ni_{22}Co_{39}/C$ nanoalloys prepared by two slightly different processes, that is "non-reactive−reductive" treatment (curve a), and "oxidative−reductive" treatment (curve b), the latter of which was the same sample shown in Figure 5 (curve a). These two samples are compared to assess the effect of the treatment condition on

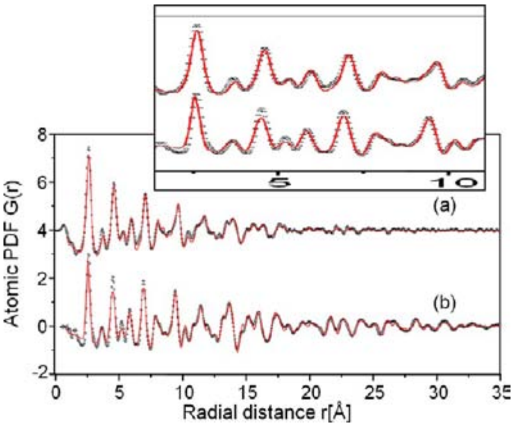

Figure 6. Atomic PDFs for $Pt_{39}Ni_{22}Co_{39}$ nanoalloys supported on carbon with two different thermal treatment conditions: (a) treatment at 260 °C in N_2 (nonreactive) followed by at 400 °C in 15 vol % H_2 (reductive); and (b) treatment at 260 °C in 15 vol % O_2 (oxidative) followed by treatment at 400 °C in 15 vol % H_2 (reductive). Results from PDF modeling (line in red) are explained in the text. (Insert: a zoomed view of the data in the lower radial distance region).

the atomic-scale structure of the catalysts. The PDFs data show that the $Pt_{39}Ni_{22}Co_{39}/C$ sample derived from the oxidative–reductive treatment (Figure 6 curve b) shows a longer length of structural coherence (about 35 Å) than the sample obtained by the nonreactive–reductive treatment (Figure 6 curve a), where the length of structural coherence is only about 20 Å.

By fitting the experimental PDFs with structure models even finer details of the atomic arrangement in the respective nanoparticles can be revealed as discussed below. The fits were done with the help of the program PDFGui.[67] Two model types were tested: chemically ordered and chemically disordered cubic-type structures that are known to exist in materials of composition close to (noble metal)(transition metal)$_3$. The archetypal structure type is $AuCu_3$.[68] The experimental PDF for $Pt_{39}Ni_{22}Co_{39}/C$ nanoalloys obtained by a oxidative–reductive treatment was best fit with a model featuring a cubic-type ordering (red line in Figure 5B curve a and Figure 6 curve b) where noble (Pt) and base transition metals (Ni/Co) atoms are randomly distributed with respect to each other. The respective fcc lattice parameter is a = 3.820 Å. On the other hand, the experimental PDF for $Pt_{39}Ni_{22}Co_{39}/C$ nanoalloys obtained by a nonreactive–reductive treatment was best fit with a model featuring a cubic-type ordering (red lines in Figure 6 curve a) where noble (Pt) and base transition metal (Ni/Co) atoms are chemically ordered with respect to each other. The respective fcc lattice parameter is a = 3.824 Å. The silica supported $Pt_{39}Ni_{22}Co_{39}$ particles (Figure 5B curve b), like the carbon supported ones obtained by a nonreactive–reductive treatment (Figure 6 curve a), show a significant local positional disorder reducing the length of structural coherence to about 20 Å. The structure type of these nanoparticles is again of a cubic-type with a lattice parameter of a = 3.84 Å. In addition, however, the particles show strong signatures of a phase segregation manifested by the presence of a pronounced low-r shoulder of the first PDF peak. The shoulder is positioned at about 2.5 Å which is a typical transition metal–transition metal first neighbor distance. The first principal PDF peak is positioned at 2.70 Å, which corresponds to Pt–Pt distances. The experimental PDF for the nanoparticles supported on titania is best fit with a model featuring a cubic-type structure with little local positional disorder manifested by a length of structural coherence of about 35 Å. The respective cubic lattice parameter is a = 3.830 Å. The first PDF peak is positioned at 2.70 Å. Within this structure, however, Pt and transition metal (Ni/Co) atoms are randomly distributed with respect to each other, rendering it a structurally quite perfect but chemically quite random type of alloy.

Visualizations of the different types of chemical ordering in the nanoalloy particles on different supports or treated by different annealing conditions studied here are shown in Figure 7. The treatment conditions clearly affect the structure type of the nanoalloy (see Figure 6). The $Pt_{39}Ni_{22}Co_{39}/C$ derived from the nonreactive–reductive treatment are structurally (length of structural coherence of only about 20 Å) quite disordered but chemically ordered. In contrast, the $Pt_{39}Ni_{22}Co_{39}/C$ sample derived from the oxidative–reductive treatment shows a structurally more perfect (length of structural coherence of about 35 Å) but chemically disordered structure that is similar to the one exhibited by the nanoalloy particles on TiO_2 support. The differences in the degree of structural coherence (i.e., degree of crystallinity) and chemical ordering/disordering, as will be summarized in Table 1, clearly impact the catalytic activity, which is evidenced by the data shown in Figure 3 for the nanoalloy/C catalysts prepared by nonreactive–reductive and the oxidative–reductive treatments.

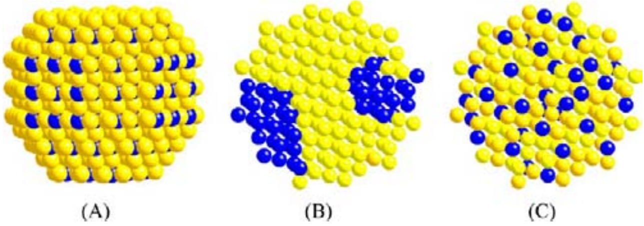

Figure 7. Chemical order–disorder effects in supported $Pt_{39}Ni_{22}Co_{39}$ nanoparticles: chemically ordered structure for the carbon-supported particles prepared by the nonoxidative–reductive treatment (A), phase segregated structure on the silica-supported particles (B), and chemically disordered (random alloy) structure for the titania-supported particles and the carbon-supported particles prepared by the oxidative–reductive treatment (C). Transition base metals are in yellow, Pt is in blue. The configurations feature cubic type ordering where the relative concentration of transition base metal atoms (Co/Ni) to Pt atoms is 3:1. The chemically ordered model is based on the archetypal (noble metal)(transition metal)$_3$ (e.g., $AuCu_3$-type) structure.

Considering the significant differences in terms of the catalytic activity and the alloying structure for the nanoalloys treated by the reactive thermal treatment conditions, the question of how the atomic-scale structure of the nanoparticles changes under oxygen oxidation and hydrogen reduction atmospheres was further addressed by in situ experiments conducted in the respective atmospheres. Figure 8 shows a set of PDFs for $Pt_{25}Ni_{16}Co_{59}/C$ catalyst that was annealed under 10 vol % O_2 (Figure 8A) and then under 5 vol % H_2 (Figure 8B) at 400 °C. It is important to note that this catalyst showed significantly enhanced activity for CO oxidation (Figure 3B). As the PDF data (curve a in Figure 8A) show the nanoalloy particles expand uniformly; that is, all interatomic distances increase when the catalyst is treated in oxidizing atmosphere catalyst (follow the broken line in Figure 8A). In contrast, the nanoalloy particles shrink uniformly; that is, all interatomic

Table 1. Summary of the Structural Parameters Determined from Atomic PDFs Analysis, the Relative Surface Composition from XPS Analysis, and the Catalytic Activity Data

$Pt_{39}Ni_{22}Co_{39}$ /support	thermochemical treatment	chemical ordering	model[a]	SNI[b]	activitve site and activity
/carbon	nonreactive−reductive	chemically ordered structure	A	weak	type-I, with low initial activity
/carbon	oxidative−reductive	chemically disordered (random alloy)	C	strong	type-I, with high initial activity
/SiO_2	oxidative−reductive	phase-segregated structure	B	weak	type-I, with medium initial activity
/TiO_2	oxidative−reductive	chemically disordered (random alloy)	C	strong	type-I, with high initial activity stabilized by type-II

[a] The chemical order−disorder models in Figure 7. [b] SNI: support-nanoalloy interaction.

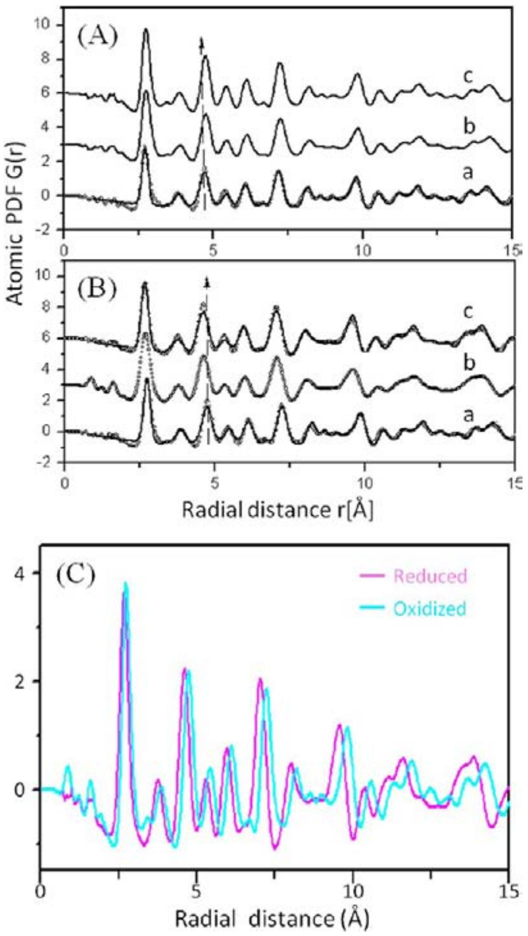

Figure 8. Atomic PDFs for $Pt_{25}Ni_{16}Co_{59}$ nanoalloys supported on carbon obtained from in situ HE-XRD data collected under controlled temperature and oxidative (O_2)/reductive (H_2) atmosphere. The catalyst was subjected sequentially to two different treatment conditions: (A) under 10 vol % O_2 (a) starting with room temperature (25 °C), (b) heating to 260 °C and (c) cooling back to room temperature; and (B) under 5 vol % H_2 (a) starting with room temperature, (b) heating to 400 °C, and (c) cooling back to room temperature. (C) Comparison of curves labeled c in panels A and B, revealing a significant difference in the positions of the PDF peaks, that is, of the interatomic distances in the samples subjected to different treatment.

distances decrease when the catalyst is treated in reducing atmosphere (follow the broken line in Figure 8B). Moreover, the nanoalloy particles remain "expanded" when cooled back to room temperature in oxidizing atmosphere, and "shrunk" if cooled back to room temperature in reducing atmosphere as the data in Figure 8C show. This is one of the first examples demonstrating the effect of gas atmosphere on the overall atomic-scale structure of ternary alloy catalysts. The expansion of the interatomic distances upon oxidation is consistent with the enhanced interaction of oxygen with the particle's surface that is favored by the oxophilicity of the base transition metal. This interaction, however, as our catalytic data show, results in a deactivation of the catalyst. The overall shrinking of the interatomic distances in the nanoalloy particles treated in a reducing atmosphere is consistent with freeing their surface from the oxygen species. As our catalytic data show this also leads to a reactivation of the catalyst.

3.3. XPS Characterization. Samples of $Pt_{39}Ni_{22}Co_{39}$ on C and TiO_2 were also examined using XPS technique to assess the relative surface composition of the nanoparticles after exposure to different annealing and gas reaction conditions (Figure 9). For the catalyst treated at 280 °C under O_2 followed by a treatment at 400 °C under H_2 (Figure 9A−E curves d), Pt $4f_{7/2}$ and Pt $4f_{5/2}$ bands were observed at 71.0 and 74.5 eV, characteristic of Pt^0. The main Ni $2p_{3/2}$ and $2p_{1/2}$ peaks were observed at 855.6 and ~861.5 eV (very weak), characteristic of oxidized Ni (+2), with a small fraction at 852.2 eV characteristic of Ni^0. The main Co $2p_{3/2}$ and $2p_{1/2}$ peaks were observed at 781.1 and ~796.5 eV (the shoulder peak at ~786 eV is due to satellite peak of Co(+2)), characteristic of oxidized Co(+2), with a small fraction at 777.9 eV characteristic of Co^0. Interestingly, these peaks did not show significant changes under different reaction conditions (260 °C under N_2 (a), 550 °C under N_2 (b), and 280 °C under O_2 (c)), indicating the Pt^0 state for Pt and oxidized state for Ni and Co. The little or small changes also suggest some "buffering" capabilities of the TiO_2 support to the components' oxidation states of the nanoalloy. By comparing the O_2 treated samples (c and d) with the N_2 treated samples (a and b), there appears a higher binding energy (BE) component (~532 eV) for the O_2 treated catalysts, in addition to the usual 529.7 eV band corresponding to the oxygen species in TiO_2. The ~532 eV band is believed to be due to the oxygenated Ni/Co species on the nanoalloy, suggesting the propensity of forming surface oxygenated metal species on the nanoalloy upon exposure of the catalyst to ambient atmosphere. This kind of oxygenated species was apparently eliminated by thermal treatment in N_2 at high temperature (550 °C) and enhanced by thermal treatment in O_2. Moreover, Ti $2p_{3/2}$ and $2p_{1/2}$ peaks observed at 459 and 465 eV are consistent with Ti(4+) in TiO_2. The peak positions showed almost no dependence on the different treatments. In comparison with the composition determined by the bulk analysis method (ICP−OES) (Pt:Ni:Co = 36:20:34), there appears to be a tendency of the nanoparticle's surface enrichment in Pt (Pt:Ni:Co = 43:30:37) depending on the thermal treatment (Supporting Information, Table S2). The XPS data show not only surface oxidation of Ni/Co components in the nanoalloy but also some enrichment of Pt on the nanoalloy's surface.

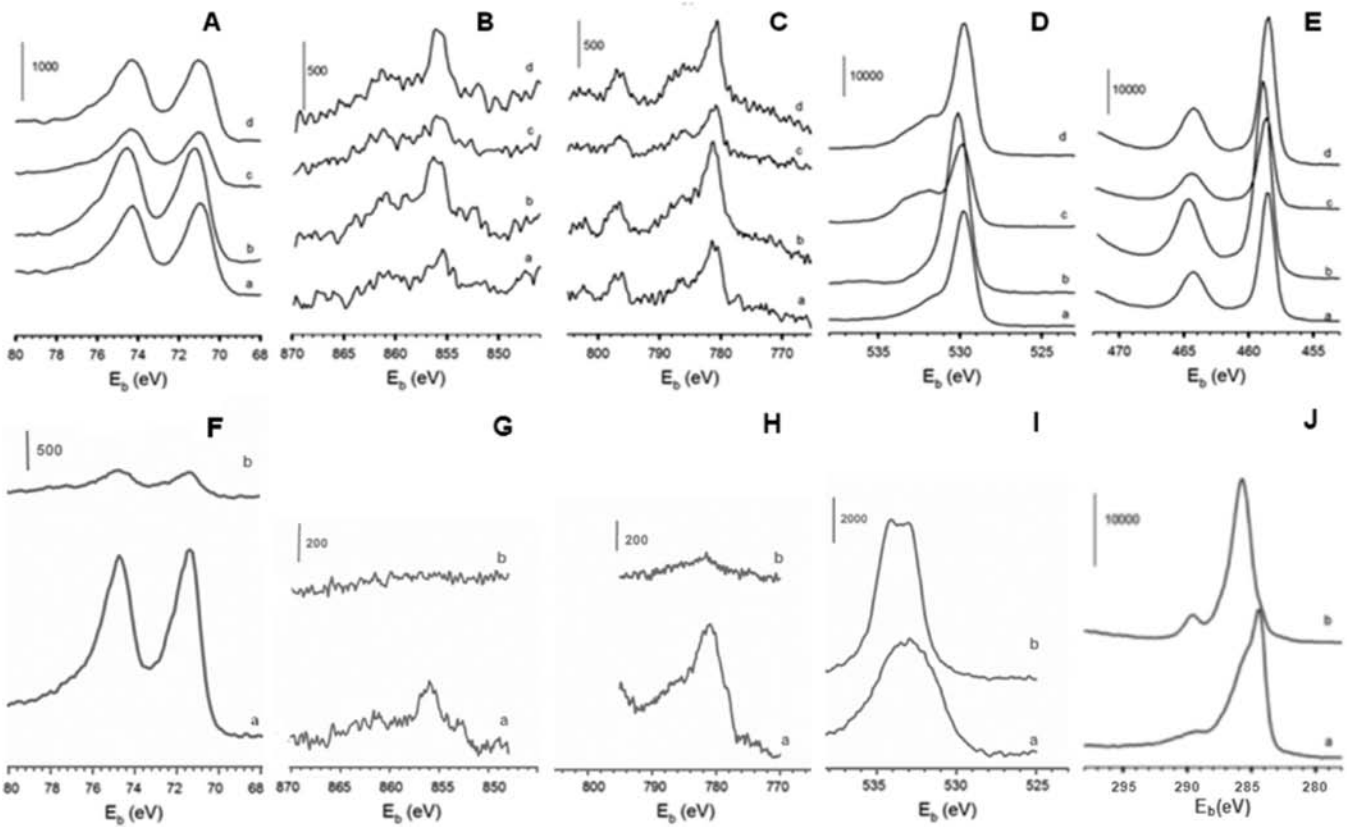

Figure 9. XPS spectra. (Top panel) Pt4f (A), Ni2p (B), Co2p (C), O1s (D), and Ti2p (E) regions for samples of $Pt_{39}Ni_{22}Co_{39}/TiO_2$ treated under several different conditions: 260 °C under N_2 (a), 550 °C under N_2 (b), 280 °C under O_2 (c), and 280 °C under O_2 followed by 400 °C under H_2 (d). (Bottom panel) Pt4f (F), Ni2p (G), Co2p (H), O1s (I), and C1s (J) regions for samples of $Pt_{39}Ni_{22}Co_{39}/C$ which was treated under O_2 at 280 °C first followed treatment under H_2 at 400 °C (a), and aged under CO + O_2 reaction (100 °C).

There are two additional findings from this set of data (Supporting Information, Table S3). First, the C1s peak for the carbon support shows a significant change with annealing and gas reaction conditions. For the as-prepared catalyst, the main C1s peak is observed at 284.4 eV, characteristic of unoxidized carbon, with shoulders at ~285.8 and ~289.7 eV indicating the presence of some oxidized states of carbon. In contrast, the catalyst exposed to a reaction atmosphere shows a main C1s peak at 285.8 eV and a small peak at ~289.7 eV, suggesting some degree of surface oxidation. Second, the O1s peak for the fresh catalyst is broad and centered at 532.4 eV, whereas the aged catalyst shows a doublet at 532.4 and 534.2 eV, both within the envelope of the broad peak observed for the fresh catalyst. The detected O1s peaks with different treatments could be assigned a combination of the oxygenated carbon species, as supported by C1s peaks at ~289 eV, and oxygenated Ni/Co species, as supported by the subtle difference of the O1s peaks (531−535 eV) between the two treatments. Moreover, the absence of O1s peak below 531 eV is indicative of the absence of lattice oxygen, ruling out the possibility of Ni/Co oxides as the active sites.

The $Pt_{39}Ni_{22}Co_{39}/C$ catalyst prepared by an initial treatment under O_2 at 280 °C followed by a treatment under H_2 at 400 °C (a) was also compared with the same catalyst after exposure to CO + O_2 reaction atmosphere at 100 °C for 20 h (Figure 9(F−J)). For the as-prepared catalyst, Pt $4f_{7/2}$ and $4f_{5/2}$ bands were observed at 71.4 and 74.7 eV, characteristic of Pt^0. The main Ni $2p_{3/2}$ and $2p_{1/2}$ peaks appear at 856.0 and ~861.7 eV (very weak), characteristic of oxidized Ni(+2), with a small fraction at 852.9 eV characteristic of Ni^0. The main Co $2p_{3/2}$ peak appears at 781.0 eV (the shoulder peak at ~786 eV is due to satellite peak of Co(+2)), characteristic of oxidized Co(+2), with a small fraction at ~778 eV characteristic of Co^0. Note, the same catalyst after being exposed to reaction atmosphere shows diminished peak intensities likely due to the small amount of the sample. Quantitatively, the relative surface composition change (Supporting Information, Table S3) suggests some degree of enrichment of Co on the nanoalloy surface and enrichment of Ni in the nanoalloy core.

3.4. Discussion on SNI and Its Effect on Structure−Activity Correlation. The above results clearly demonstrate that nanosized alloys of Pt with base transition metals (Co or Ni) exhibit a remarkable synergistic catalytic activity on the CO oxidation reaction that varies with the chemical nature of the support and SNI as a result of the annealing treatment. Metal and titania support are known to have a strong interaction due to M−Ti(3+) and/or metal-vacancy interaction, whereas metal and silica have a weak interaction due to a high stability of the tetrahedron structure.[47−49] On the basis of this understanding, a pure carbon surface should have a weak interaction with metals due to a lack of any specific bonding, whereas carbon with surface oxygenated functional groups could have a strong interaction with metal due to their reactivities. A key difference for these variations in SNI's strength is reflected by the nanoalloy's atomic-scale structural/chemical ordering which defines Type-I active sites. Table 1 summarizes some of the key findings for the nanoalloys on the three different supports.

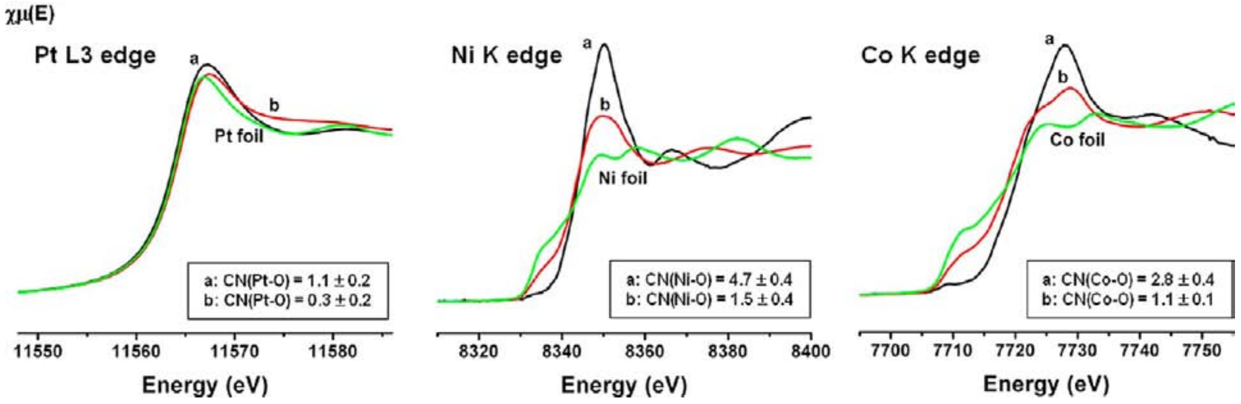

Figure 10. XANES spectra at Pt L3 edge, Ni K edge and Co K edge for $Pt_{39}Ni_{22}Co_{39}/C$ catalysts treated at (a) 260 °C in 15 vol % O_2 (oxidative atmosphere) only and (b) 15 vol % O_2 (oxidative atmosphere) followed by treatment at 400 °C in 15 vol % H_2 (reductive atmosphere).

As shown by the atomic PDFs, atoms in all three nanoalloy catalysts studied here arrange in a close packed, cubic type ordering. That fcc ordering suffers local distortions in the nanoalloys supported on carbon, especially in the case of nonreactive−reductive treatment, and on silica, as manifested by their substantially reduced length of structural coherence: 25 Å and 30 Å, respectively. It is less distorted in the titania supported nanoalloy particles where the length of structural coherence extends to 35 Å. Furthermore, the way Pt and base transition metal atoms arrange across the nanoalloys is different for the different supports. In the case of silica support the Pt and base transition metal atoms tend to phase segregate. They form a chemically-disordered or ordered type alloy on the carbon support in the case of oxidative−reductive and nonreactive−reductive treatment, respectively, and a chemically-random type alloy on the titania support. The implication of this distinctive type of chemical ordering on the catalytic activity can be rationalized as follows: Because of the phase segregation the base transition metal (M/M′) and Pt atoms in the nanoalloy particles supported on silica are quite separated from each other which may result in their surfaces being separated into distinct M/M′ and Pt domains (Figure 7B). In the carbon supported particles of a chemically ordered structure type, M/M′ and Pt atoms alternate in layers of two distinct types: entirely occupied with M/M′ atoms, and occupied with M/M′ and Pt atoms in a 50:50 ratio (chemically ordered $CuAu_3$ alloy type). This chemically ordered atomic structure may result in the nanoparticle's surface being terminated with either type of layers/facets (Figure 7A). For titania support, Pt and M/M′ atoms are randomly alloyed (chemically disordered $CuAu_3$ alloy type), which may result in their surface being populated with more or less a random mixture of M/M′ and Pt atoms in a ratio close to 3 to 1. This type of chemical disordering, that is, the abundant presence of M-Pt-M′ sites, and the fact that these particles suffer very little structural distortions may promote the formation of Type-I active sites for oxygen activation. Note that it is known that large structural disorder often has an adverse effect on the catalytic properties of metallic particles.[69] This structurally well-ordered and chemically-disordered nanoalloy (see Figure 7C) is in sharp contrast with the chemically phase-segregated catalyst on the silica support, where M/M′ and Pt are largely separated making it impossible for M-Pt-M′ sites to operate in large numbers (Figure 7B). The carbon-supported nanoalloys show an overall structural and chemical disordering/ordering of M/M′ and Pt atoms in between these two limiting cases (Figure 7A), which explains its intermediate catalytic activity.

Consider now the surface modification of the nanoalloys under the different treatment conditions. In our recent study[61] using a combination of XANES and XPS techniques, the surface oxygenated metal species were shown to be highly dependent on the thermal treatment condition. In comparison with predominant oxygenated metal species in the oxidatively treated sample, the oxidative−reductive treatment revealed a significant reduction of the oxygenated metal species which were formed upon exposure of the catalysts to ambient conditions after the treatment. As shown by the XANES spectra in Figure 10A, the detected change in the oxygenated Pt species from the oxidative to the oxidative−reductive treatments was very small. In contrast, significant changes are observed for Ni and Co (Figure 10B,C), showing much less oxygenated Ni and Co species for the oxidative−reductive treatment than that for oxidative treatment. In addition to indicating an important role played by oxidation treatment of the nanoalloy, the detected changes in coordination numbers translate to an increased degree of alloying, in an excellent agreement with the HE-XRD data analysis here and the previous EXAFS analysis,[61] and a decreased oxygenated Ni/Co species in the nanoalloy after the oxidative−reductive treatment.

Similar results have also been obtained from the XANES data for as-prepared PtNi/C and PtCo/C catalysts (see Supporting Information, Figure S3). While the amount of oxygenated Co in PtCo is similar to that in PtNiCo, interestingly the extent of forming oxygenated Ni in PtNi appears to be less than that in PtNiCo. This subtle difference further substantiates the difference between binary and ternary nanoalloys in terms of the formation of oxygenated base metals, suggesting a synergistic balance in forming oxygenated species between Co and Ni in the ternary system. This finding is consistent with our explanation of the activity data shown in Figure 2.

This assessment was substantiated by XPS analysis of the nanoalloys,[61] revealing a significant decrease in the oxygenated metal species in the nanoalloy derived from the oxidative−reductive treatment. The XPS analysis showed a clear decrease in the amount of detected oxygen species with increasing O_2% in the oxidative treatment which was followed by the reductive treatment, indicating that the oxygenated species originate largely from the nanoalloy surface.

From the results and discussions above it is becoming clear that different supports and treatment conditions affect substantially both the overall atomic-scale structure of the

Scheme 2. Illustration of the Proposed Catalytic CO Reaction on a Supported Nanoalloy Catalyst in Either Reduced Nanoalloy (A) or Oxidized Nanoalloy (B) States, Involving Oxygen Storage and Release Capacity Where the Transition Base Metals Ni/Co Provide Sites for the Activated O^{2-} and $O^{\delta-}$ Species[a]

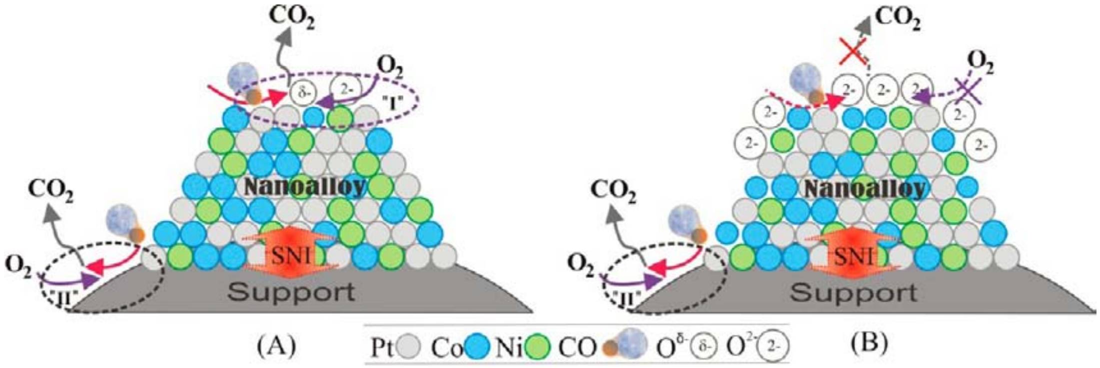

[a]The support−nanoalloy interaction (SNI) is indicated by the arrow between the two materials. While both cases may involve Type-II sites for O_2 activation, the Type-I site for O_2 activation exists only on the reduced nanoalloy surface (Case A) and does not exist on the oxidized nanoalloy surface where the surface is completely blocked by the oxide species (Case B).

nanoalloy particles and the surface oxygenated Ni/Co species. It is the combination of the particle's atomic-scale structural/chemical ordering and the surface chemistry that determines the nanoalloy's catalytic activity. As illustrated in Scheme 2, nanoalloy particles alone can provide Type-I sites (Co−Pt−Ni sites) involving Pt atoms for activating CO and base transition metal atoms (Ni/Co) for assisting the oxygen activation. Supports like titania can provide extra catalyst−support perimeter sites (Type-II sites), which are inactive in the case of silica supports and hardly available in the case of carbon supports. Oxygen activation is crucial for the CO oxidation, which can occur on both the surface Pt−Co/Ni active sites (Type-I) of the nanoalloy particle and the anionic deficiency sites (Type-II) of the support for the catalysts, thus substantially influencing the overall reaction rate. For the reduced nanoalloys (Scheme 2A), the differences among the catalytic activities of the three supported catalysts cannot be explained in terms of Type-II sites since silica and carbon supports do not have them.

When the surface is covered by Co/Ni oxide species, Type-I sites are basically blocked (Scheme 2B). This is consistent with the poor activities of all three oxidized catalysts, even in the case of TiO_2 support where Type-II sites are present. Thus, if the fraction of surface base metals is significant, then the blocking will be more serious, which explains the observation of the propensity of deactivation of the carbon catalysts containing a higher percentage of base metals. The origin for the differences among the catalysts on the three different supports then can mainly come from Type-I sites. These sites and the degree of Co−Pt−Ni bonds' local disorder are very much influenced by SNI. A strong SNI, as in the case of TiO_2, favors the formation of structurally ordered (i.e., with a low degree of local atomic positional disorder) but chemically disordered (i.e., with a random distribution of the base transition metals and Pt species with respect to each other) nanoalloys. This leads to an enhanced population of Co−Pt−Ni (Type-I) sites for effective oxygen activation. A weaker SNI, on the other hand, leaves more room for local structural distortions and rearrangement of the chemical species with respect to each other. The nanoalloys could undergo structural evolution upon the thermochemical treatment (see Figure 6), in which Co−Pt−Ni (Type-I) sites rearrange to influence the catalytic activity, as in the case of carbon-supported nanoalloys. For a weak SNI, as is the case with silica support, the chemical species in the ternary nanoalloys segregate, which diminishes the Co−Pt−Ni (Type-I) sites and resulting in a decreased catalytic activity. Qualitatively, we believe that it is the thermodynamic balance of the adhesion energy of the nanoparticles on the support and the nanoscale metal−metal bonding energy which constitutes the driving force for alloying or phase segregation. The latter was in fact substantiated by both experimental and theoretical assessments for different nanoparticle systems (e.g., AuPt nanoparticles[12,13,21]), whereas the former is partially supported by studies of metal particles mobility and sintering of gold nanoparticles on different substrates.[70,71] Quantitative probing of the driving force is part of our ongoing effort.

4. CONCLUSION

The results have demonstrated that the combination of the ternary Pt−Ni−Co composition in the nanoalloy leads to enhanced activity and stability can be enhanced, in which Co promotes the activity whereas Ni is responsible for the stability enhancement. Importantly, the atomic-scale structure, in particular the degree of structural and chemical ordering, in the alloy nanoparticles can be significantly affected by SNI and further modified by controlled thermochemical treatment. For the supported nanoalloy, the atomic-scale structure that ensures an enhanced catalytic activity features cubic type ordering with little atomic positional disorder where the base transition metal and Pt atomic species are randomly arranged with respect to each other. This atomic-scale structural evolution is favored by titania supports, providing Type-I active sites on the nanoalloy in addition to Type-II active sites from the nanoalloy-support perimeter zone. By controlled thermochemical treatment this type of structure can also be achieved for the nanoalloys on carbon support. The lack of Type-II sites on the carbon support, however, could not sustain the high initial catalytic activity from Type-I sites. This type of structure is not favored by silica supports and the formation of Type-I active sites is thus suppressed, which, together with the lack of Type-II active sites, results in the lowest activity for the silica-supported nanoalloys. Taken together, our findings highlight the importance of oxygen-activation active sites on the nanoalloy surface and point to a strategy for tuning such active sites by exploiting SNI with various supports. The findings are significant for desigining highly acitve catalysts for various catalytic oxidation reactions. In the case of desigining catalysts for PROX, in which H_2 is present during the catalytic CO oxidation reaction,[42−46] it is anticipated that our proposed catalytic Type-I sites would function with an enhanced effectiveness. Our findings also demonstrate the importance of combining traditional analytical techniques with nontraditional high-energy XRD coupled to atomic PDFs analysis in revealing the important details of the atomic-scale structure of nanoalloy catalysts, and so providing a knowledge base for guiding the design and preparation of active catalysts with a wide range of nanoalloy compositions.

■ ASSOCIATED CONTENT

Ⓢ Supporting Information

Additional figures and tables as described in the text. This material is available free of charge via the Internet at http://pubs.acs.org.

■ AUTHOR INFORMATION

Corresponding Author

cjzhong@binghamton.edu; petkov@phy.cmich.edu

Notes

The authors declare no competing financial interest.

■ ACKNOWLEDGMENTS

This work was supported by the DOE-BES Grants DE-SC0006877, and in part by the National Science Foundation (CBET-0709113). Work at the Advanced Photon Source was supported by DOE under Contract DE-AC02-06CH11357. Thanks are also due to 11IDB beamline staff for the help with the in situ XRD experiments. The XAFS work at the 9-BM Beamline was also supported by DOE. The XPS analysis was performed using EMSL, a national scientific user facility sponsored by the DOE's Office of Biological and Environmental Research and located at Pacific Northwest National Laboratory.

■ REFERENCES

(1) Gasteiger, H. A.; Kocha, S. S.; Sompalli, B.; Wagner, F. T. *Appl. Catal. B* **2005**, *56*, 9−35.

(2) Zhong, C. J.; Luo, J.; Njoki, P. N.; Mott, D.; Wanjala, B.; Loukrakpam, R.; Lim, S.; Wang, L.; Fang, B.; Xu, Z. C. *Energy Environ. Sci.* **2008**, *1*, 454−466.

(3) Stamenkovic, V. R.; Mun, B. S.; Arenz, M.; Mayrhofer, K. J. J.; Lucas, C. A.; Wang, G. F.; Ross, P. N.; Markovic, N. M. *Nat. Mater.* **2007**, *6*, 241−247.

(4) Stamenkovic, V.; Schmidt, T. J.; Ross, P. N.; Markovic, N. M. *J. Electroan. Chem.* **2003**, *554*, 191−199.

(5) Paulus, U. A.; Wokaun, A.; Scherer, G. G.; Schmidt, T. J.; Stamenkovic, V.; Radmilovic, V.; Markovic, N. M.; Ross, P. N. *J. Phys. Chem. B* **2002**, *106*, 4181−4191.

(6) Greeley, J.; Stephens, I. E. L.; Bondarenko, A. S.; Johansson, T. P.; Hansen, H. A.; Jaramillo, T. F.; Rossmeisl, J.; Chorkendorff, I.; Norskøv, J. K. *Nat. Chem.* **2009**, *1*, 552−556.

(7) Stamenkovic, V. R.; Fowler, B.; Mun, B. S.; Wang, G. F.; Ross, P. N.; Lucas, C. A.; Markovic, N. M. *Science* **2007**, *315*, 493−497.

(8) Stamenkovic, V.; Schmidt, T. J.; Ross, P. N.; Markovic, N. M. *J. Phys. Chem. B* **2002**, *106*, 11970−11979.

(9) Mukerjee, S.; Srinivasan, S.; Soriaga, M. P.; McBreen, J. *J. Electrochem. Soc.* **1995**, *142*, 1409−1422.

(10) Toda, T.; Igarashi, H.; Uchida, H.; Watanabe, M. *J. Electrochem. Soc.* **1999**, *146*, 3750−3756.

(11) Toda, T.; Igarashi, H.; Watanabe, M. *J. Electroanal. Chem.* **1999**, *460*, 258−262.

(12) Wanjala, B. N.; Luo, J.; Loukrakpam, R.; Fang, B.; Mott, D.; Njoki, P. N.; Engelhard, M.; Naslund, H. R.; Wu, J. K.; Wang, L. C.; Malis, O.; Zhong, C. J. *Chem. Mater.* **2010**, *22*, 4282−4294.

(13) Wanjala, B. N.; Luo, J.; Fang, B.; Mott, D.; Zhong, C. J. *J. Mater. Chem.* **2011**, *21*, 4012−4020.

(14) Loukrakpam, R.; Luo, J.; He, T.; Chen, Y.; Xu, Z.; Njoki, P. N.; Wanjala, B. N.; Fang, B.; Mott, D.; Yin, J.; Klar, J.; Powell, B.; Zhong, C. J. *J. Phys. Chem. C* **2011**, *115*, 1682−1694.

(15) Loukrakpam, R.; Chang, P.; Luo, J.; Fang, B.; Mott, D.; Bae, I. T.; Naslund, H. R.; Engelhard, M. H.; Zhong, C. J. *Chem. Commun.* **2010**, *46*, 7184−7186.

(16) Wanjala, B. N.; Loukrakpam, R.; Luo, J.; Njoki, P. N.; Mott, D.; Zhong, C. J.; Shao, M. H.; Protsailo, L.; Kawamura, T. *J. Phys. Chem. C* **2010**, *114*, 17580−17590.

(17) Fang, B.; Luo, J.; Chen, Y.; Wanjala, B. N.; Loukrakpam, R.; Hong, J.; Yin, J.; Hu, X.; Hu, P.; Zhong, C. J. *ChemCatChem* **2011**, *3*, 583−593.

(18) Fang, B.; Wanjala, B. N.; Hu, X. A.; Last, J.; Loukrakpam, R.; Yin, J.; Luo, J.; Zhong, C. J. *J. Power Sources* **2011**, *196*, 659−665.

(19) Fang, B.; Luo, J.; Njoki, P. N.; Loukrakpam, R.; Wanjala, B.; Hong, J.; Yin, J.; Hu, X.; Last, J.; Zhong, C. J. *Electrochim. Acta* **2010**, *55*, 8230−8236.

(20) Fang, B.; Luo, J.; Njoki, P. N.; Loukrakpam, R.; Mott, D.; Wanjala, B.; Hu, X.; Zhong, C. J. *Electrochem. Commun.* **2009**, *11*, 1139−1141.

(21) Luo, J.; Han, L.; Kariuki, N. N.; Wang, L. Y.; Mott, D.; Zhong, C. J.; He, T. *Chem. Mater.* **2005**, *17*, 5282−5290.

(22) Luo, J.; Kariuki, N.; Han, L.; Wang, L.; Zhong, C. J.; He, T. *Electrochim. Acta* **2006**, *51* (23), 4821−4827.

(23) He, T.; Kreidler, E.; Xiong, L.; Luo, J.; Zhong, C. J. *J. Electrochem. Soc.* **2006**, *153* (9), A1637−A1643.

(24) Luo, J.; Wang, L. Y.; Mott, D.; Njoki, P. N.; Kariuki, N.; Zhong, C. J.; He, T. *J. Mater. Chem.* **2006**, *16*, 1665−1673.

(25) Wei, Z. D.; Feng, Y. C.; Li, L.; Liao, M. J.; Fu, Y.; Sun, C. X.; Shao, Z. G.; Shen, P. K. *J. Power Sources* **2008**, *180*, 84−91.

(26) Yu, P.; Pemberton, M.; Plasse, P. *J. Power Sources* **2005**, *144*, 11−20.

(27) Tamizhmani, G.; Capuano, G. A. *J. Electrochem. Soc.* **1994**, *141*, 968−975.

(28) Mani, P.; Srivastava, R.; Strasser, P. *J. Power Sources* **2011**, *196*, 666−673.

(29) Seo, A.; Lee, J.; Han, K.; Kim, H. *Electrochim. Acta* **2006**, *52*, 1603−1611.

(30) Shim, J.; Yoo, D. Y.; Lee, J. S. *Electrochim. Acta* **2000**, *45*, 1943−1951.

(31) Chen, Y. S.; Fulton, J. L.; Partenheimer, W. *J. Solution Chem.* **2005**, *34*, 993−1007.

(32) Ravel, B.; Newville, M. *J. Synchrotron Rad.* **2005**, *12*, 537−541.

(33) Newville, M. *J. Synchrotron Rad.* **2001**, *8*, 96−100.

(34) Rehr, J. J.; Albers, R. C. *Rev. Mod. Phys.* **2000**, *72*, 621−654.

(35) Arico, A. S.; Shukla, A. K.; Kim, H.; Park, S.; Min, M.; Antonucci, V. *Appl. Surf. Sci.* **2001**, *172*, 33−40.

(36) Shukla, A. K.; Neergat, M.; Bera, P.; Jayaram, V.; Hegde, M. S. *J. Electroanal. Chem.* **2001**, *504*, 111−119.

(37) Shukla, A. K.; Raman, R. K.; Choudhury, N. A.; Priolkar, K. R.; Sarode, P. R.; Emura, S.; Kumashiro, R. *J. Electroanal. Chem.* **2004**, *563*, 181−190.

(38) Yang, D. Q.; Sacher, E. *J. Phys. Chem. C* **2009**, *113*, 6418−6425.

(39) Nurmi, J. T.; Tratnyek, P. G.; Sarathy, V.; Baer, D. R.; Amonette, J. E.; Pecher, K.; Wang, C. M.; Linehan, J. C.; Matson, D. W.; Penn, R. L.; Driessen, M. D. *Environ. Sci. Technol.* **2005**, *39*, 1221−1230.

(40) Mathieu, H. J.; Landolt, D. *Corros. Sci.* **1986**, *26*, 547−559.

(41) Wanjala, B. N.; Fang, B.; Luo, J.; Chen, Y.; Yin, J.; Engelhard, M.; Loukrakpam, R.; Zhong, C. J. *J. Am. Chem. Soc.* **2011**, *133*, 12714−12727.

(42) Selim, A.; Anand, U. N.; Manos, M.; Eichhorn, B. *Nat. Mater.* **2008**, *7*, 333−338.
(43) Graham, J. H. *Dalton Trans.* **2008**, *41*, 5523−5536.
(44) Liu, X.; Wang, A.; Wang, X.; Mou, C. Y.; Zhang, T. *Chem. Commun.* **2008**, *27*, 3187−3189.
(45) Bracey, C. L.; Ellis, P. R.; Hutchings, G. *J. Chem. Soc. Rev.* **2009**, *38*, 2231−2243.
(46) Wang, C.; Li, B.; Lin, H.; Yuan, Y. *J. Power Sources* **2012**, *202*, 200−208.
(47) Mihaylov, M.; Hadjiivanov, K.; Knozinger, H. *Phys. Chem. Chem. Phys.* **2006**, *8*, 407−417.
(48) Tauster, S. J. *Acc. Chem. Res.* **1987**, *20*, 389−394.
(49) Haruta, M. *Nature* **2005**, *437*, 1098−1099.
(50) Schalow, T.; Brandt, B.; Starr, D. E.; Laurin, M.; Shaikhutdinov, S. K.; Schauermann, S.; Libuda; Freund, J. H.-J. *Angew. Chem., Int. Ed.* **2006**, *45*, 3693−3697.
(51) Green, I. X.; Tang, W.; Neurock, M.; Yates, J. T., Jr. *Science* **2011**, *333*, 736−739.
(52) Valden, M.; Lai, X.; Goodman, D. W. *Science* **1998**, *281*, 1647−1650.
(53) Chen, M. S.; Goodman, D. W. *Science* **2004**, *306*, 252−255.
(54) Herzing, A. A.; Kiely, C. J.; Carley, A. F.; Landon, P.; Hutchings, G. J. *Science* **2008**, *321*, 1331−1335.
(55) Guzman, J.; Carrettin, S.; Corma, A. *J. Am. Chem. Soc.* **2005**, *127*, 3286−3287.
(56) He, T.; Kreidler, E.; Xiong, L. F.; Ding, E. R. *J. Power Sources* **2007**, *165*, 87−91.
(57) Shi, X.; Luo, J.; Njoki, P.; Lin, Y.; Lin, T. H.; Mott, D.; Lu, S.; Zhong, C. J. *Ind. Eng. Chem. Res.* **2008**, *47*, 4675−4682.
(58) Greeley, J.; Nørskov, J. K. *J. Phys. Chem. C* **2009**, *113*, 4932−4939.
(59) Nørskov, J. K.; Rossmeisl, J.; Logadottir, A.; Lindqvist, L.; Kitchin, J. R.; Bligaard, T.; Jónsson, H. *J. Phys. Chem. B* **2004**, *108*, 17886−17892.
(60) Wang, C.; Li, D.; Chi, M.; Pearson, J.; Rankin, R. B.; Greeley, J.; Duan, Z.; Wang, G.; van der Vliet, D.; More, K. L.; Markovic, N. M.; Stamenkovic, V. R. *J. Phys. Chem. Lett.* **2012**, *3*, 1668−1673.
(61) Wanjala, B.; Fang, B.; Loukrakpam, R.; Chen, Y; Engelhard, M.; Luo, J.; Yin, J.; Yang, L; Shan, S; Zhong, C. J. *ACS Catal.* **2012**, *2*, 795−806.
(62) Egami, T.; Billinge, S. J. L. *Underneath the Braggs' Peak* (Pergamon/Amsterdam, Netherlands, 2003).
(63) Petkov, V. *Mater. Today* **2008**, *11*, 28−38.
(64) Oxford, S. M.; Lee, P. L.; Chupas, P. J.; Chapman, K. W.; Kung, M. C.; Kung, H. H. *J. Phys. Chem. C* **2010**, *114*, 17085−17091.
(65) Petkov, V.; Bedford, N.; Knecht, M. R.; Weir, M. G.; Crooks, R. M.; Tang, W.; Henkelman, G.; Frenkel, A. *J. Phys. Chem. C* **2008**, *112*, 8907−8911.
(66) Huang, W. J.; Sun, R.; Tao, J.; Menard, L. D.; Nuzzo, R. G.; Zuo, J. M. *Nat. Mater.* **2008**, *7*, 308−313.
(67) Farrow, C. L.; Juhás, P.; Liu, J. W.; Bryndin, D.; Božin, E. S.; Bloch, J.; Proffen, Th.; Billinge, S. J. L. *J. Phys.: Condens. Matter* **2007**, *19*, 335219−7.
(68) Proffen, Th.; Petkov, V.; Billinge, S. J. L.; Vogt, T. *Z. Kristallogr.* **2002**, *217*, 47−50.
(69) Sun, Y.; Zhuang, L.; Lu, J.; Hong, X.; Liu, P. *J. Am. Chem. Soc.* **2007**, *129*, 15465−15467.
(70) Luo, J.; Jones, V. W.; Maye, M. M.; Han, L.; Kariuki, N. N.; Zhong, C. J. *J. Am. Chem. Soc.* **2002**, *124*, 13988−13989.
(71) Luo, J.; Jones, V. W.; Han, L.; Maye, M. M.; Kariuki, N. N.; Zhong, C. J. *J. Phys. Chem. B* **2004**, *108*, 9669−9677.